InSAR Digital Surface Model Refinement by Block Adjustment with Horizontal Constraints

Lai Wei [1], Tao Ke [1, 2, *], Quan Jing [3], Fanhong Li [3], Pengjie Tao [1, 2]

[1] School of Remote Sensing and Information Engineering, Wuhan University, Wuhan 430079, China – (whuweilai, ketao, pjtao)@whu.edu.cn
[2] Hubei Luojia Laboratory, Wuhan 430079, China
[3] Institution of Remote Sensing Satellite, Chinese Academy of Space Technology, Beijing, China - springf6@hotmail.com, fanhonglee@pku.edu.cn

Keywords: Block Adjustment, Digital Surface Model, InSAR, ICESat-2.

ABSTRACT

Interferometric Synthetic Aperture Radar (InSAR) technology is an important method to generate digital surface model (DSM). The past studies on space-borne derived DSM most focused on the elevation correction, due to the relative low resolution of DSM product. As a large number of high-resolution satellite data emerge, the horizontal discrepancies are needed to be considered. This paper proposes a DSM block adjustment method with horizontal constraints, aimed at eliminating the horizontal errors that exist between multiple DSM scenes with overlaps, achieving high precision and consistency in both the horizontal and vertical dimensions. Using ICESat-2 ATL08 point clouds as absolute elevation control and a reference DSM for horizontal control, the adjustment equations are constructed based on the constraint of tie points and controls. The experiment selects 7 image pairs of China TH2-01 SAR satellite, corresponding ICESat-2 ATL08 point and AW3D30 as reference DEM. The block adjustment results show that the proposed method improves the absolute vertical accuracy from 3.78 m to 2.56 m and reduces the average horizontal standard deviation between the InSAR derived DSMs and the reference AW3D30 from 15.31 m to 9.08 m.

1. Introduction

Digital surface model (DSM) has played a fundamental role in the field of remote sensing (Okolie and Smit, 2022) and photogrammetry (Cao et al., 2019). And it becomes increasingly integral in various fields, from hydrodynamic modelling (Jarihani et al., 2015) to landslide detection (Qiu et al., 2022). The reconstruction of large-scale DSM from satellite imagery is a widely used method, primarily divided into DSM reconstruction from optical satellite imagery (Hu et al., 2024) and Interferometric Synthetic Aperture Radar (InSAR) technology (Jakob J., 2001). In scenarios such as cloud coverage and night time, InSAR has certain advantages, due to its 'day and night' and its 'all-weather' observation capability. However, InSAR technology itself has limitations. The accuracy of InSAR-derived DSM is affected by factors such as orbital positioning, registration of SAR images, and phase unwrapping. Therefore, it is necessary to refine DSM to increase its utilisation value and benefit the processing of editing DSM to DEM.

DSM accuracy is influenced by several factors including the source data attributes, sensor distortions, land cover types and terrain, errors inherent in the methods used for generating the DSMs. Crosetto (2002) uses an adequate number of evenly distributed ground control points (GCPs) and low-resolution height data to improve the DSM accuracy, making the standard deviation of vertical error of ERS-1 DSM dropped from 18.1 m to 11.4 m. However, only the height information of the GCPs was used for control, ignoring the horizontal constraints. Chen and Yue (2010) has shown that the total errors of DSMs are actually composed of sampling, interpolation and terrain representation errors. A DSM block adjustment method has been proposed during the TanDSM-X mission (Gruber et al., 2009, 2012; Wessel et al., 2009, 2018). Wessel et al. (2009) approximately expresses these systematic error characteristics by a third order polynomial. The application of DSM block adjustment can significantly improve the relative elevation accuracy between adjacent DSMs (Gruber et al., 2012). However, for the block adjustment, it is assumed that each DSM acquisition is solely distorted by systematic error in vertical. The Ice, Cloud, and Land Elevation Satellite (ICESat) data is used as absolute height reference. The ICESat space-borne laser altimeter data provide globally distributed, accurate height information as well as evaluation and classification information for each measurement point (Zwally et al., 2002). Arefi and Reinartz (2011) uses ICESat to refine ASTER GDEM by comparing the ICESat points with ASTER GDEM interpolated points to remove the vertical offsets. After launched in 2018, ICESat-2 operates with three pairs of beams, each pair separated by about 3 km cross-track with a pair spacing of 90 m. Each of the beams will have a nominal 17 m diameter footprint with an along-track sampling interval of 0.7 m (Markus et al., 2017). Li et al. (2023) constructed a regression model to correct GDEM and SRTM elevation values by using ICESat-2 altimetry data. Xu et al. (2010) uses DSM difference surfaces and outlier filtering. Kim et al. (2020) analyses the relationship between their vertical accuracies and land/topographic parameters (e.g., land use/ land cover, slope, aspect), the magnitude and distribution of the vertical error can be modelled and minimised.

However, previous studies have only utilized the elevation information of auxiliary data, and very few of them consider the constraints of the tie points in the overlapping areas. For the block adjustment method in Wessel et al. (2009), they directly bind the horizontal positions of the ICESat points to the grids at the corresponding position on the DSMs for elevation correction, ignoring the impact of the discrepancies between the DSMs and ICESat points. For high resolution SAR satellite system (S. Li et al., 2022), the assumption in Wessel et al. (2009) needs to be reconsidered. And Shean et al. (2016) shows that a translation is always needed to remove both horizontal and vertical bias when processing with very high resolution commercial stereo satellite imagery. With the increasing demand for high-resolution DSM

---

[*] Corresponding author

products, both horizontal and vertical accuracy need to be taken into account (Shean et al., 2016).

This paper proposes a DSM refinement method by block adjustment with horizontal constraints that considers both the horizontal and vertical refinement of the InSAR derived DSM. Based on the analysis of the error characteristics of the space-borne InSAR derived DSM, a block adjustment method for InSAR derived DSM is constructed. The method utilizes ICESat-2 laser data as the absolute height constraint and reference DSM products as the reference horizontal constraint, aiming to evaluate and produce a high-precision DSM product.

2. Methodology

The proposed DSM block adjustment with horizontal constraints processing flow is shown in Figure 1.
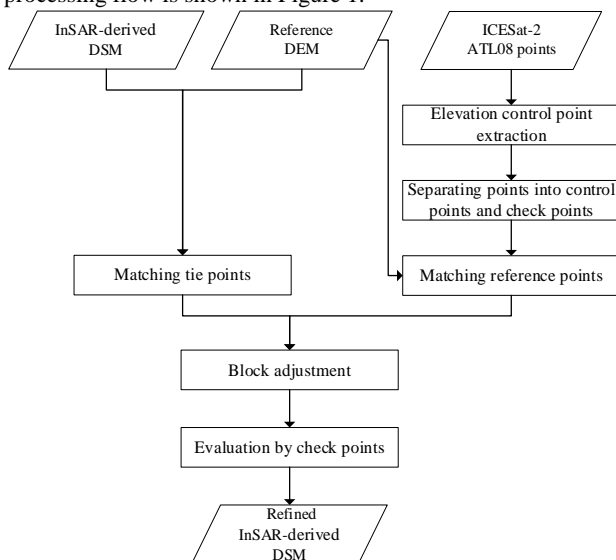

Figure 1. Flowchart of the proposed DSM block adjustment with horizontal constraints

The process can be generally divided into four parts: laser elevation control points extraction, matching between DSMs for tie points and reference points, block adjustment with horizontal constraints, and accuracy evaluation.

2.1 ICESat-2 Laser Points Extraction

Since launched in 2018, several extraction and accuracy evaluation methods for vertical control points from ICESat-2 has been proposed (Li et al., 2021; Shang et al., 2022). The ICESat-2 data is processed into 22 levels of data products, which are named as ATL00–ATL21. Among them, the ATL03 is the global geolocated photon cloud after various geophysical corrections are introduced. The ATL08 is extracted from the ATL03 data after filtering and classification, which contains heights for both terrain and canopy at 100 m segments in the along-track direction and other descriptive parameters generated from the measurements. Compared with ATL03, ATL08 is more efficient to be processed and contains more descriptive parameters for support. We select ATL08 to be the source of laser data for the laser point extraction, and the vertical root mean square error (RMSE) of the extracted points can be smaller than 1 m. We adopt the following vertical control points extraction strategy.

Figure 2 shows the extraction steps. The eight steps can be divided into two categories: the first category is extraction by attributes, and the second is extraction by statistical analysis. The details of the steps are described as follow:
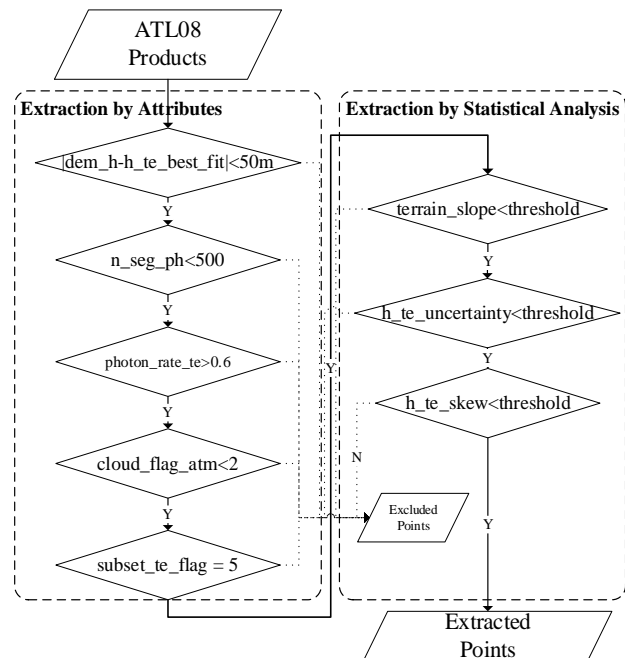

Figure 2. Overall flowchart of the proposed elevation control points extraction strategy

1) dem_h & h_te_best_fit: For eliminating the outliers by a comparison with DEM/DSM data, the threshold was set according to the accuracy of popular reference DEM (Li et al., 2021; Shang et al., 2022). 2) n_seg_ph: A huge number of photons may indicate that there would be more noise photons (generated by atmospheric or high reflectivity land cover). 3) photon_rate_te: To ensure the accuracy of fitting terrain elevation, the ratio of terrain photos in the segment is on demand. 4) cloud_flag_atm: If the value is greater than 0, there would be layers of aerosols or cloud. 5) subset_te_flag: To guarantee the fitting accuracy, we hope the terrain photons to be evenly distributed in the horizontal direction of the segment. We require all 5 sub-segments within the segment having terrain photons. 6) terrain_slope: In flat areas (slope < 2∘), the accuracy of ICESat-2 is highest and decreases with slope increasing. The slope threshold is set according to the requirements of the accuracy and the terrain condition of experiment area. 7) h_te_uncertainty: The threshold is set according to the required accuracy of the extracted points, the points with higher h_te_uncertainty will be excluded. 8) h_te_skew: Skewness is an indicator that measures the asymmetry of a probability distribution. If a distribution is completely symmetric, then its skewness is 0. The description of the labels used in the extraction is shown in Table 1.

Label	Description
dem_h	Best reference DEM value at the position.
h_te_best_fit	The best fit terrain elevation at the mid-point location of each 100m segment.
n_seg_ph	Number of photons within each segment.
photon_rate_te	Calculated photon rate of terrain photons.
cloud_flag_atm	Cloud confidence flag indicating the number of cloud or aerosol layers.
subset_te_flag	Indicates whether all five sub-segments within the segment have terrain photons.
terrain_slope	The along-track slope of terrain.
h_te_uncertainty	Uncertainty of the mean terrain height.
h_te_skew	The skewness of the photon heights.

Table 1. The description of the labels used in the extraction.

Considering the better measurement accuracy of ICESat-2 points in areas with small slope (slope < 2°), the distribution of the vertical control points will be concentrated in the flat areas. This situation will alleviate the vertical errors caused by the horizontal inconsistency between the vertical control points and the DEM. On the other side, excessively dense points cannot significantly improve the block adjustment results and will introduce redundant computation, since the dense points share similar elevations. Therefore, we select vertical control points by choosing one point within a certain radius. After the application of vertical control points extraction strategy and selection, the initial high-precision vertical control points will be extracted and divided into two categories, control points and validation points.

2.2 Matching for Tie Points and Reference Points

For the block adjustment, the tie points and control points are needed. Ravanbakhsh and Fraser (2013) compares several DSM registration methods, and recommends the mutual information (MI) method using entropy (Shannon, 1948). The method uses image intensity or gradient information to detect and describe feature points; however, both intensity and gradient are not distinctive in the intensity form of DSM. For the purpose of enhancing image features, we introduce the hillshading technique. The hillshading is a technique for visualizing terrain determined by a light source and the slope and aspect of the elevation surface. It is a qualitative method for visualizing topography and does not give absolute elevation values. After the application of hillshading, we use the Radiation-Variation Insensitive Feature Transform (RIFT) method (Li et al., 2020) to obtain the tie points and reference points. The flowchart of the DSM match method is shown by Figure 3.
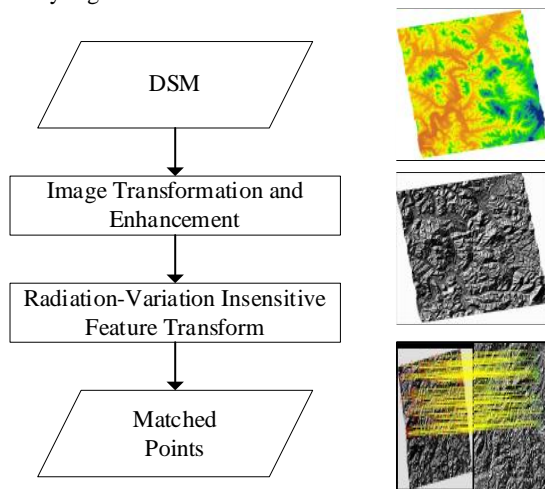

Figure 3. The flowchart of the DSM match method.

2.3 Block Adjustment

The purpose of the block adjustment is to align the DSMs on both horizontal and vertical dimensions. The constraint of vertical adjustment is that the heights in overlapping areas and on control laser point should be identical:

$$\begin{cases} \widetilde{H}_{i,j} = \widetilde{H}_{i,k} \\ \widetilde{H}_{m,j} = \widetilde{H}_m \end{cases} \quad (1)$$

where $\widetilde{H}_{i,j}$, $\widetilde{H}_{i,k}$ are the true heights of the i-th tie points on DSM j and k, respectively. $\widetilde{H}_m$ denotes the elevation of the m-th ATL08 elevation control point, $\widetilde{H}_{m,j}$ denotes its true height of the corresponding tie point in DSM j.

We use a second order polynomial to approximately express the systematic errors of elevation:

$$g_j(x,y) = a_j + b_j x + c_j y + d_j x * y + e_j x^2 + f_j y^2 \quad (2)$$

where, a_j, b_j, c_j, d_j, e_j, f_j are the DSM j's unknown parameters to be solved, (x,y) are image coordinates.

Then the true height of i-th tie points on DSM j is described as below:

$$\widetilde{H}_{i,j} = H_{i,j} + g_j(x_i, y_i) \quad (3)$$

where $H_{i,j}$ denotes the measured height values from the DSM j, $g_j(x_i, y_i)$ denotes the compensation height of i-th tie points on (x_i, y_i) of DSM j. Taking the systematic errors into account, Equation (1) would change into:

$$\begin{cases} H_{i,j} - H_{i,k} + g_j(x_i, y_i) - g_k(x_i, y_i) = 0 \\ H_{m,j} - \widetilde{H}_m + g_j(x_i, y_m) = 0 \end{cases} \quad (4)$$

Since the ICESat-2 points only have latitude and longitude coordinates, it is essential to unite the horizontal position of ICESat-2 points and InSAR-derived DSM. The reference DSM is used to evaluate and uniform the horizontal position:

$$\begin{cases} X_{i,j} = X_{i,k} \\ Y_{i,j} = Y_{i,k} \\ X_{m,j} = X_m \\ Y_{m,j} = Y_m \end{cases} \quad (5)$$

where $(X_{i,j}, Y_{i,j})$ denotes the geographical coordinates of tie points on DSM j, $(X_{i,k}, Y_{i,k})$ denotes the corresponding tie point geographical coordinates on DSM k. $(X_{m,j}, Y_{m,j})$ denotes the geographical coordinates of reference points in DSM j, (X_m, Y_m) denotes the corresponding tie point geographical coordinates on the reference DSM. The DSMs with larger horizontal discrepancy will have a small weight in the calculation:

$$w_j = \frac{1}{|\bar{\sigma} - \sigma_j|} \quad (6)$$

where w_j denotes the weight of DSM j, $\bar{\sigma}$ denotes the mean of RMSE of the horizontal discrepancy of all DSMs to the reference DSM, σ_j denotes the RMSE of horizontal discrepancy of DSM j to the reference DSM.

Joining the above equations (4) – (6), by applying the principle of least squares, the elevation systematic errors of each DSM are alleviated, yielding the coefficients for the error correction model and the correction numbers for the six positioning parameters of each DSM image. This results in a refined DSM with unified corrections for elevation and horizontal errors.

2.4 Evaluation Method

We use the RMSE as the quantified measures to evaluate discrepancy values in both horizontal and vertical direction. The RMSE is defined as

$$\sigma_Z = \sqrt{\frac{1}{p} \sum_{i=1}^{p} (H_i - \widetilde{H}_i)^2} \quad (7)$$

$$\sigma_{XY} = \sqrt{\frac{1}{q}\sum_{i=1}^{q}[(X_i - \hat{X}_i)^2 + (Y_i - \hat{Y}_i)^2]} \qquad (8)$$

Where, i denotes the point index, p represents the total number of ICESat-2 elevation control points, and q represents the total number of matched reference points. $\tilde{H}_i$ represent the elevation of i-th ICESat-2 elevation control points, and $(\hat{X}_i, \hat{Y}_i)$ denotes the geographical coordinates of i-th matched reference points on the reference DSM. It's worth noting that horizontal accuracy serves solely as a constraint for the vertical adjustment, and the horizontal accuracy depends on the type of the reference DSM.

3. Experiment

3.1 Datasets and Experimental Setup

We selected seven InSAR image pairs obtained by TH2-01 SAR satellite with overlapping coverage, captured between June 2020 and October 2021. The TH2-01 satellite was launched on April 30, 2019, equipped with the high resolution SAR and the high precision inter satellite relative state measurement equipment and other payloads, which was able to obtain all-day and all-weather InSAR image data. TH2-01 is a bistatic SAR satellite system information flight, it can eliminate decoherent sources such as time and atmosphere. Therefore, TH2-01 can generate highly coherent SAR image pairs. Wang et al. (2022) evaluated the ground target positioning accuracy of TH2-01 satellite, which can achieve a RMSE of 2 m. The method described in Xiang et al. (2022) was used to generate DSM from SAR image pairs.

We chose ICESat-2 ATL08 data from the same period and region, coming from 76 photographic missions. Li et al. (2022) investigated the accuracies of three most recently released 1-arcsec global DEMs (GDEMs, Copernicus, NASA and AW3D30) through ICESat-2 ATL08 points, and (Uuemaa et al., 2020) compared freely available global DEMs (ASTER, AW3D30, MERIT, TanDEM-X, SRTM, and NASA DEM) by high precision LiDAR and Pleiades-1A DEMs. The results show that the AW3D30 showed the smallest uncertainty and highest accuracy across most study areas. In this paper, the AW3D30 with 30 m resolution was selected as reference DSM. The coverage of the DSM is shown in Figure 4. We use the cubic interpolation method to resample the reference DSM AW3D30 resolution to 10 m, which is the same resolution of derived DSM.
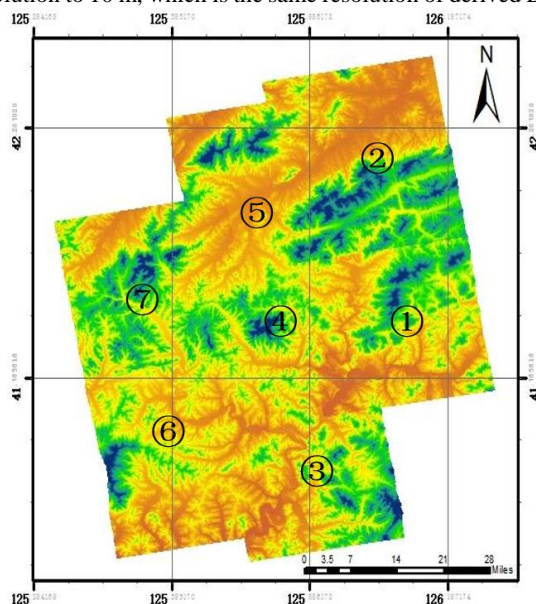

Figure 4. Overview of DSMs derived from TH2-01 image pairs.

3.2 Laser Point Extraction

The filtering thresholds for terrain_slope, h_te_uncertainty, and h_te_skew are set to 0.05, 1 m, and 1, respectively. After the extraction, 3132 points are remained. The remained ATL08 points are divided into 1792 control points and 1340 validation points, with the search radius set to 120 m. The distribution of the control points and the validation points is shown in Figure 5.
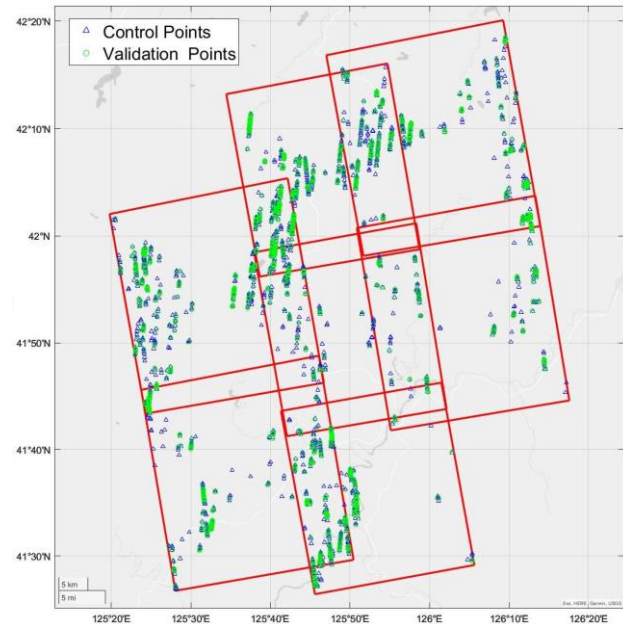

Figure 5. ICESat-2 ATL08 points after extraction

The details of the extraction and division are shown in Table 2. The application of photon_rate_te, n_seg_ph and terrain_slope contributes most in the extraction, eliminating 23.49%, 20.85% and 14.19% of the laser points, respectively.

Labels	Number	Retention Rate
Total Laser Points	11860	100.00 %
dem_h & h_te_best_fit	10968	92.48 %
n_seg_ph	8495	71.63 %
photon_rate_te	5709	48.14 %
cloud_flag_atm	5205	43.89 %
subset_te_flag	5096	42.97 %
terrain_slope	3413	28.78 %
h_te_uncertainty	3391	28.59 %
h_te_skew	3132	26.41 %
Total Extracted Points	3132	100.00 %
Control Points	1792	57.22 %
Validation Points	1340	42.78 %

Table 2. The details of point extraction and point categories.

3.3 Evaluation of Horizontal Accuracy

The matched DSM is converted into a grayscale image using the hillshade function of Geospatial Data Abstraction Library (GDAL/OGR contributors, 2024). The result of the image matching is shown in Figure 6, and 7813 pairs of corresponding points were obtained between all the seven InSAR DSM scenes.
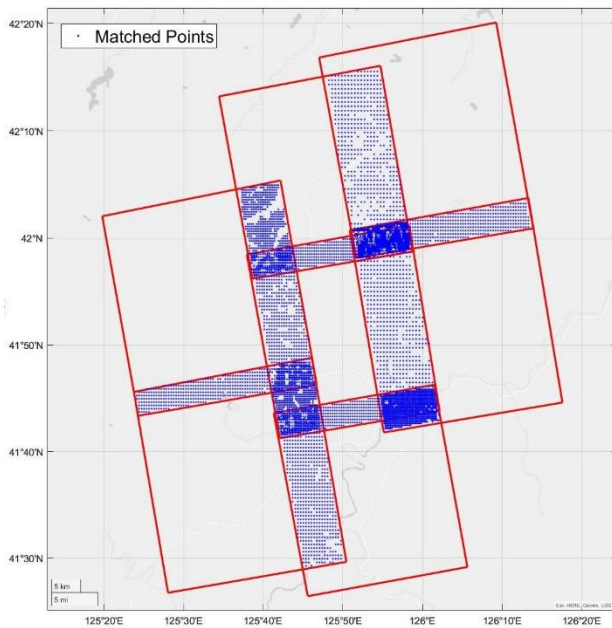
Figure 6. The distribution of tie points between DSMs

Figure 7 shows the horizontal discrepancies of the matched tie points; the different colours denote the different set of tie points. As can be seen from the figure, the distribution of horizontal errors within each strip shows as random error, and exhibits systematic errors between strips.
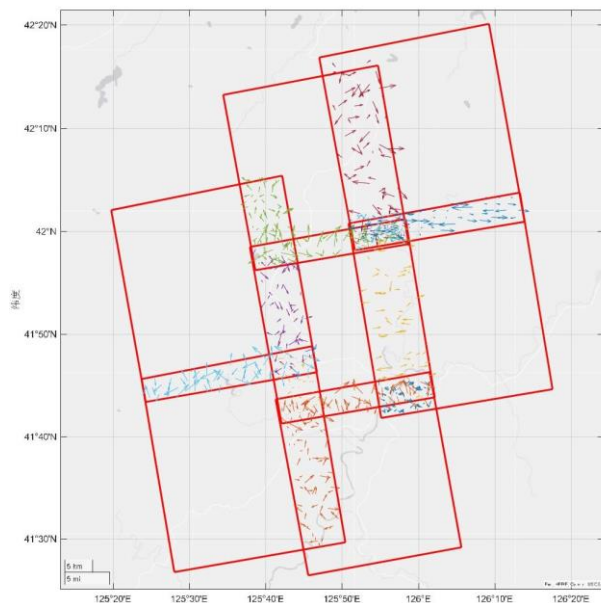

Figure 7. The horizontal discrepancies of the tie points, represent the length and direction of horizontal differences by vector. The different colours denote the different set of tie points.

With the AW3D30 as the reference DSM, the horizontal discrepancies of the matched reference points are shown in Figure 8; the different colours denote the different set of reference points. The horizontal discrepancies of after horizontal adjustment are shown in Figure 9. And the statistical of the reference points is shown in Table 3. From Figure 8, it is evident that although the reference DSM has a lower original resolution than the InSAR derived DSMs, the reference DSM could find out the difference of the InSAR derived DSMs' horizontal position accuracies. The σ_X, σ_Y and σ_{XY} between all the InSAR derived

DSMs and the reference DSM are 7.01 m, 13.62 m and 15.31 m, respectively. The coordinated of the InSAR derived DSMs and the reference DSM have systematic errors, while the systematic errors vary between the InSAR derived DSM. Compared to the latitude direction, the DSMs exhibit higher consistency in the longitude direction, σ_Y is twice as large as σ_X. As shown in Figure 8, the distribution of horizontal discrepancy of scene 3 is different from those of others. And the horizontal discrepancy between scene 3 and scene 5 in the latitudinal direction is about 11 m, which is larger than one pixel's extent. The horizontal consistency varies within different strips, the strip of scenes 3-5 exhibits a lower horizontal consistency to another two strips. After the horizontal adjustment, σ_X, σ_Y and σ_{XY} between DSMs and the reference DSM drop to 5.82 m, 6.96 m and 9.08 m. As can be seen from the Figure 9, the DSMs' horizontal position accuracies are more consistent.
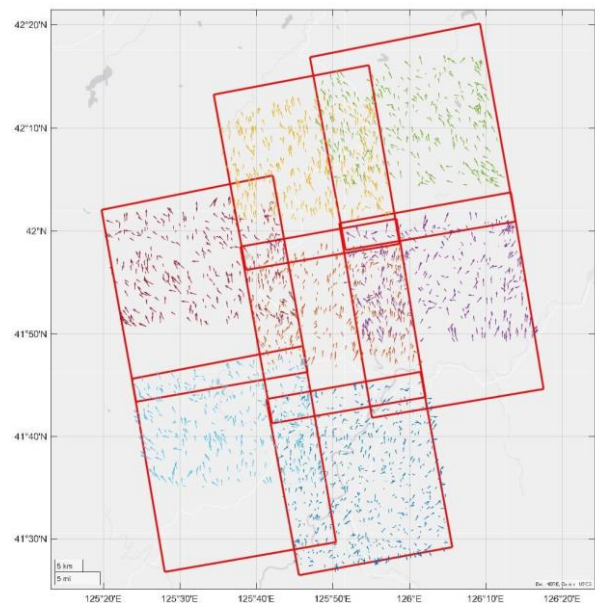

Figure 8. The horizontal discrepancies of the reference points, represent by vector. The different colours denote the different set of reference points.
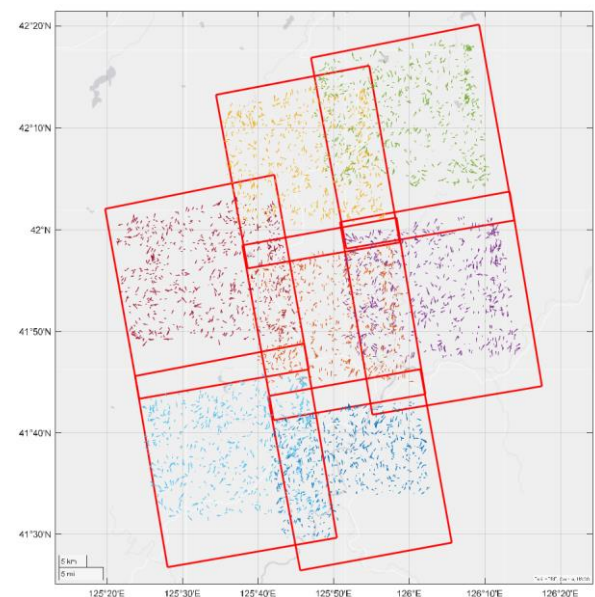

Figure 9. The horizontal discrepancies of the reference points after horizontal adjustment, represent by vector. The different colours denote the different set of reference points.

Scenes	Without horizontal adjustment			With horizontal adjustment		
	σ_X (m)	σ_Y (m)	σ_{XY} (m)	σ_X (m)	σ_Y (m)	σ_{XY} (m)
1	4.52	10.99	12.51	5.93	7.74	9.53
2	7.65	14.75	17.58	6.54	6.87	9.48
3	5.76	8.55	10.31	5.21	7.23	8.91
4	5.09	14.60	15.46	4.82	6.49	8.08
5	6.27	19.55	20.53	5.40	6.95	8.80
6	6.06	12.45	14.53	6.12	6.74	9.10
7	6.39	14.48	16.96	6.56	7.02	9.61
Overall	7.01	13.62	15.31	5.82	6.96	9.08

Table 3. The horizontal accuracies of the test seven InSAR derived DSM from TH2-01.

3.4 Evaluation of Vertical Accuracy

The original vertical accuracies of the test seven InSAR derived DSM from TH2-01 are shown in Table 4.

Scenes	$mean_{\triangle Z}$ (m)	σ_Z (m)
1	1.68	3.57
2	1.48	2.92
3	3.92	5.60
4	4.05	5.38
5	3.18	3.73
6	1.65	3.38
7	1.14	2.19
Overall	2.34	3.78

Table 4. The original vertical accuracies of the test seven InSAR derived DSM from TH2-01.

The overall mean value and σ_Z are 2.34 m and 3.78 m. The mean value and σ_Z of scenes 3, 4 and 5 are much larger than others, which is about 2.5 times and 1.5 times larger, respectively. Excluding scenes 3-5, the mean value and σ_Z of remaining scenes can reach 1.51 m and 3.02 m. Combined with the horizontal evaluation of section 3.3, we can see that the strip is more inconsistent in horizontal direction, the σ_Z of DSM within in the strip is larger.

Compare the elevation accuracies of 3 Schemes, the original InSAR DSMs without constraint (Scheme 1), using only vertical constraint of the extracted ATL08 points (Scheme 2), and using vertical & horizontal constraints of both extracted ATL08 points and the control points on the reference DSM simultaneously (Scheme 3). The result is shown in Table 5. When using vertical constraint, the σ_Z of absolute accuracy drops from 3.78 m to 2.66 m. The application of horizontal constraint brings 0.1 m improvement to σ_Z.

	Condition	σ_Z (m)
Scheme 1	Without constraint	3.78
Scheme 2	Vertical constraint	2.66
Scheme 3	Vertical & horizontal constraint	2.56

Table 5. The results of elevation accuracy.

The Figure 10 shows the distribution of vertical difference. The vertical constraint makes the distribution of vertical differences concentrated and alleviates systematic offsets. The application of vertical & horizontal constraint makes the distribution of vertical differences more concentrated.
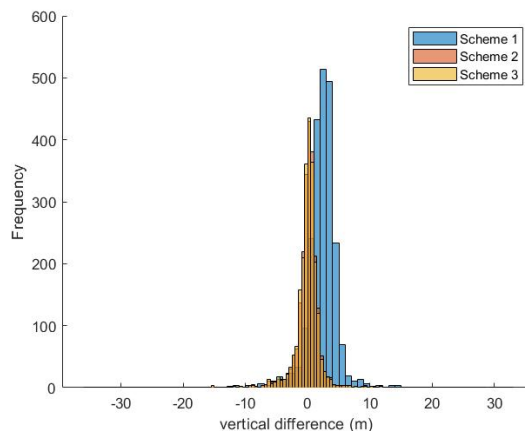

Figure 10. The distribution of vertical difference.

4. Conclusion

This paper proposes a DSM block adjustment method with horizontal constraints, aimed at alleviating the horizontal errors and the vertical errors, caused by horizontal errors, between multiple DSM scenes, and ultimately obtaining a DSM product with high precision in both the horizontal and vertical dimensions. Using ICESat-2 ATL08 point clouds as absolute vertical control and a reference DSM for horizontal control, the adjustment equations are constructed based on the constraint of tie points and control points in both horizontal and vertical directions. The average σ_X, σ_Y and σ_{XY} between the InSAR derived DSMs and the reference AW3D30 are respectively 7.01 m, 13.62 m and 15.31 m, and they vary between the DSMs. After the horizontal adjustment, σ_X, σ_Y and σ_{XY} between DSMs and the reference DSM drop to 5.82 m, 6.96 m and 9.08 m. The DSMs' horizontal position accuracies are more consistent. The block adjustment results show that the proposed method improves the absolute vertical accuracy from 3.78 m to 2.56 m. The application of horizontal constraint brings 0.1 m improvement to the solely vertical constraint of ATL08 laser points. The results show that the alleviation of horizontal errors can benefit vertical refinement of DSM, emphasizing the essential of our work.

Future work will be carried out in three aspects: (1) For the modelling of systematic elevation errors in various source DSMs, this paper is currently test on InSAR derived DSMs and will continue to research the error distribution of multi-source DSMs. (2) The reference DSM used in this experiment is an open access product with a lower resolution than the DSM to be processed. We will evaluate the method with diverse reference DSM. (3) The ICESat-2 laser points also have its horizontal errors, the application and evaluation of using ICESat-2 laser points as multiple controls is to be researched.

References

Arefi, H., and Reinartz, P., 2011. Accuracy Enhancement of ASTER Global Digital Elevation Models Using ICESat Data. *Remote Sensing* 3(7):1323–1343. doi.org/10.3390/rs3071323.

Cao, H., Tao, P., Li, H., and Shi, J., 2019. Bundle Adjustment of Satellite Images Based on an Equivalent Geometric Sensor Model with Digital Elevation Model. *ISPRS Journal of Photogrammetry and Remote Sensing* 156:169–183. doi.org/https://doi.org/10.1016/j.isprsjprs.2019.08.011.

Chen, C., and Yue, T., 2010. A Method of DEM Construction and Related Error Analysis. *Computers & Geosciences* 36(6):717–725. doi.org/10.1016/j.cageo.2009.12.001.

Crosetto, M., 2002. Calibration and Validation of SAR Interferometry for DEM Generation. *Image Spectroscopy and Hyperspectral Imaging (Special Section)* 57(3):213–227. doi.org/10.1016/S0924-2716(02)00107-7.

GDAL/OGR contributors, 2024. GDAL/OGR Geospatial Data Abstraction Software Library. Open Source Geospatial Foundation. https://doi.org/10.5281/zenodo.5884351

Gruber, A., Wessel, B., and Huber, M., 2009. TanDEM-X DEM Calibration: Correction of Systematic DEM Errors by Block Adjustment. *2009 IEEE International Geoscience and Remote Sensing Symposium* 2: II-761-II-764.

Gruber, A., Wessel, B., Huber, M., and Roth, A., 2012. Operational TanDEM-X DEM Calibration and First Validation Results. *Innovative Applications of SAR Interferometry from Modern Satellite Sensors* 73:39–49. doi.org/10.1016/j.isprsjprs.2012.06.002.

Hu, Z., Tao, P., Long, X., and Wang, H., 2024. Shading Aware DSM Generation from High Resolution Multi-View Satellite Images. *Geo-Spatial Information Science* 27(2):398–407. doi.org/10.1080/10095020.2022.2125837.

Jakob J., van Z., 2001. The Shuttle Radar Topography Mission (SRTM): A Breakthrough in Remote Sensing of Topography. *Acta Astronautica* 48(5):559–565. doi.org/10.1016/S0094-5765(01)00020-0.

Jarihani, A.A., Callow, J.N., McVicar, T.R., Van Niel, T.G., and Larsen, J.R., 2015. Satellite-Derived Digital Elevation Model (DEM) Selection, Preparation and Correction for Hydrodynamic Modelling in Large, Low-Gradient and Data-Sparse Catchments. *Journal of Hydrology* 524:489–506. doi.org/10.1016/j.jhydrol.2015.02.049.

Kim, D.E., Liong, S.-Y., Gourbesville, P., Andres, L., and Liu, J., 2020. Simple-Yet-Effective SRTM DEM Improvement Scheme for Dense Urban Cities Using ANN and Remote Sensing Data: Application to Flood Modeling. *Water* 12(3). doi.org/10.3390/w12030816.

Li, B., Xie, H., Liu, S., Tong, X., Tang, H., and Wang, X., 2021. A Method of Extracting High-Accuracy Elevation Control Points from ICESat-2 Altimetry Data. *Photogrammetric Engineering & Remote Sensing* 87(11):821–830. doi.org/10.14358/PERS.21-00009R2.

Li, B., Xie, H., Tong, X., Tang, H., and Liu, S., 2023. A Global-Scale DEM Elevation Correction Model Using ICESat-2 Laser Altimetry Data. *IEEE Transactions on Geoscience and Remote Sensing* 61:1–15. doi.org/10.1109/TGRS.2023.3321956.

Li, H., Zhao, J., Yan, B., Yue, L., and Wang, L., 2022. Global DEMs Vary from One to Another: An Evaluation of Newly Released Copernicus, NASA and AW3D30 DEM on Selected Terrains of China Using ICESat-2 Altimetry Data. *International Journal of Digital Earth* 15(1):1149–1168. doi.org/10.1080/17538947.2022.2094002.

Li, J., Hu, Q., and Ai, M., 2020. RIFT: Multi-Modal Image Matching Based on Radiation-Variation Insensitive Feature Transform. *IEEE Transactions on Image Processing* 29:3296–3310. doi.org/10.1109/TIP.2019.2959244.

Li, S., Ye, Y., Fan, W., Cong, L., Gao, J., and Shao, L., 2022. A Brief Analysis of the Positioning Accuracy for the TH-2 Satellite System. *ActaGeodaetica et Cartographica Sinica* 51:2481–2492. doi.org/10.11947/j.AGCS.2022.20210397.

Markus, T., Neumann, T., Martino, A., Abdalati, W., Brunt, K., Csatho, B., Farrell, S., Fricker, H., Gardner, A., Harding, D., Jasinski, M., Kwok, R., Magruder, L., Lubin, D., Luthcke, S., Morison, J., Nelson, R., Neuenschwander, A., Palm, S., Popescu, S., Shum, C., Schutz, B.E., Smith, B., Yang, Y., and Zwally, J., 2017. The Ice, Cloud, and Land Elevation Satellite-2 (ICESat-2): Science Requirements, Concept, and Implementation. *Remote Sensing of Environment* 190:260–273. doi.org/10.1016/j.rse.2016.12.029.

Okolie, C.J., and Smit, J.L., 2022. A Systematic Review and Meta-Analysis of Digital Elevation Model (DEM) Fusion: Pre-Processing, Methods and Applications. *ISPRS Journal of Photogrammetry and Remote Sensing* 188:1–29. doi.org/10.1016/j.isprsjprs.2022.03.016.

Qiu, H., Zhu, Y., Zhou, W., Sun, H., He, J., and Liu, Z., 2022. Influence of DEM Resolution on Landslide Simulation Performance Based on the Scoops3D Model. *Geomatics, Natural Hazards and Risk* 13(1):1663–1681. doi.org/10.1080/19475705.2022.2097451.

Ravanbakhsh, M., and Fraser, C., 2013. A Comparative Study of DEM Registration Approaches. *Journal of Spatial Science* 58(1):79–89. doi.org/doi.org/10.1080/14498596.2012.759091.

Shang, D., Zhang, Y., Dai, C., Ma, Q., and Wang, Z., 2022. Extraction Strategy for ICESat-2 Elevation Control Points Based on ATL08 Product. *IEEE Transactions on Geoscience and Remote Sensing* 60:1–12. doi.org/10.1109/TGRS.2022.3218750.

Shannon, C.E., 1948. A Mathematical Theory of Communication. *The Bell System Technical Journal* 27(3):379–423. doi.org/10.1002/j.1538-7305.1948.tb01338.x.

Shean, D.E., Alexandrov, O., Moratto, Z.M., Smith, B.E., Joughin, I.R., Porter, C., and Morin, P., 2016. An Automated, Open-Source Pipeline for Mass Production of Digital Elevation Models (DEMs) from Very-High-Resolution Commercial Stereo Satellite Imagery. *ISPRS Journal of Photogrammetry and Remote Sensing* 116:101–117. doi.org/10.1016/j.isprsjprs.2016.03.012.

Uuemaa, E., Ahi, S., Montibeller, B., Muru, M., and Kmoch, A., 2020. Vertical Accuracy of Freely Available Global Digital Elevation Models (ASTER, AW3D30, MERIT, TanDEM-X, SRTM, and NASADEM). *Remote Sensing* 12(21):3482. doi.org/10.3390/rs12213482.

Wang, S., Meng, X., Lou, L., Chen, G., Qian, F., and Liu, Z., 2022. Target Location Performance Evaluation of Single SAR Image of TH-2 Satellite System. *ActaGeodaetica et Cartographica Sinica* 51:2501–2507. doi.org/10.11947/j.AGCS.2022.20210329.

Wessel, B., Gruber, A., Huber, M., and Roth, A., 2009. TanDEM-X: Block Adjustment of Interferometric Height Models. *Proceedings of the ISPRS Hannover Workshop 2009" High-Resolution Earth Imaging for Geospatioal Information", International Archives of the Photogrammetry, Remote Sensing and Spatial Information Sciences.*

Wessel, B., Huber, M., Wohlfart, C., Marschalk, U., Kosmann, D., and Roth, A., 2018. Accuracy Assessment of the Global TanDEM-X Digital Elevation Model with GPS Data. *ISPRS Journal of Photogrammetry and Remote Sensing* 139:171–182. doi.org/10.1016/j.isprsjprs.2018.02.017.

Xiang, J., Lu, X., Fu X., Xue, F., Yun, Y., Ye, Y., and He, K., 2022. Bistatic InSAR Interferometry Imaging and DSM Generation for TH-2. *ActaGeodaetica et Cartographica Sinica* 51:2493–2500. doi.org/10.11947/j.AGCS.2022.20210323.

Xu, C., Wei, M., Griffiths, S., Mercer, B., and Abdoullaev, R., 2010. Hybrid DEM Generation and Evaluation from Spaceborne Radargrammetric and Optical Stereoscopic DEMs. *Proc. of Canadian Geomatics Conference.*

Zwally, H.J., Schutz, B., Abdalati, W., Abshire, J., Bentley, C., Brenner, A., Bufton, J., Dezio, J., Hancock, D., Harding, D., Herring, T., Minster, B., Quinn, K., Palm, S., Spinhirne, J., and Thomas, R., 2002. ICESat's Laser Measurements of Polar Ice, Atmosphere, Ocean, and Land. *Journal of Geodynamics* 34(3):405–445. doi.org/10.1016/S0264-3707(02)00042-X.